Wavelet Multi-resolution Analysis of Initial Condition Effects on Near-wake Turbulent Structures

Li, H.*1 and Zhou, Y.*2

*1   Department of Mechanical Engineering, Kagoshima University, 1-21-40, Korimoto, Kagoshima 890-0065, Japan.
*2   Department of Mechanical Engineering, The Hong Kong Polytechnic University, Hung Hom, Kowloon, Hong Kong.

Abstract: The effects of initial conditions on turbulence structures of various scales in a near wake have been investigated for two wake generators with the same characteristic dimension, i.e., a circular cylinder and a screen of 50% solidity, based on the wavelet multi-resolution analysis. The experimental investigation used two orthogonal arrays of sixteen X-wires, eight in the (x, y)-plane, and eight in the (x, z)-plane. Measurements were made at x/h (x is the streamwise distance downstream of the cylinder and h is the height of the wake generator) = 20. The wavelet multi-resolution technique was applied to decomposing the velocity data, obtained in the wakes generated by the two generators, into a number of wavelet components based on the central frequencies. The instantaneous sectional streamlines and vorticity field were thus 'visualized' for each wavelet component or central frequency. It was found that the behavior of large- and intermediate-scale structures depend on the initial conditions and the small-scale structures are independent of the initial conditions. The contributions from the wavelet components to the time-averaged Reynolds stresses and vorticity were estimated. Both the large-scale and intermediate longitudinal structures make the most significant contributions to Reynolds stresses in the circular cylinder wake, but the contribution from the large-scale structures appears dominating in the screen wake. The relatively small scale structures of the circular cylinder wake contribute most to the total rms spanwise vorticity.

Keywords: orthogonal wavelet transform, wavelet multi-resolution analysis, initial condition, turbulent structure, wake.

1. Introduction

In the past decade, there has been a growing interest in the use of wavelet analysis for turbulent structures (Farge, 1992; Li, 1998). This technique can track turbulent structures in terms of time and scale, and extracts new information on turbulence structures of various scales. The continuous wavelet transform has been applied to analyzing turbulent structures in terms of time and scale by Li and Nozaki (1995) and Li (1998). This technique is capable of extracting continuously the characterization of local regularity, but it fails to reconstruct the original function from wavelet composition because of the non-orthogonal mother wavelet function. On the other hand, the discrete wavelet transform allows an orthogonal projection on a minimal number of independent modes and is invertible. Such analysis can produce a multi-resolution representation and might be also used to analyze turbulent structures of various scales. Charles (1991) first used the one-dimensional discrete wavelet transform to obtain local energy spectra and the flux of kinetic energy from experimental and direct numerical simulation data. Staszewski et al. (1997) identified the turbulent structures of the atmospheric boundary-layer using the discrete wavelet transform. Li et al. (2000 and 2001a) employed discrete wavelet transforms to evaluate eddy structures of a jet in terms of time and scale. Li et al. (1999, 2001b) also applied the two-dimensional orthogonal wavelets to

turbulent images, and extracted the multi-resolution turbulent structures. Farge et al. (1999) developed a coherent vortex simulation method to decompose turbulent flows into coherent and incoherent structures based on orthogonal wavelets.

It is now well established that the topology and transport characteristics of the turbulent structure in the wake depend on the wake-generating bodies or initial conditions (Screenivasan, 1981; Wygnanski et al., 1986; Louchez et al., 1987; Matsumura et al., 1991; Zhou and Antonia, 1995). A number of investigators have studied the effect of the initial conditions on the behavior of a near turbulent wake. Screenivasan (1981) found substantial differences in the manner wakes produced by different wake-generating bodies, even if the mean velocity profile exhibited the same shape. A dependence of the normalized distributions of the longitudinal turbulence intensity on the initial conditions was examined by Wygnanski et al. (1986). Although Louchez et al. (1987) and Matsumura et al. (1991) have confirmed that the vortical behavior in the wake differs as the initial conditions differ; this difference has not been well documented. Zhou and Antonia (1994a) studied turbulent near-wake vortices behind various wake-generating bodies and observed a significant variation in the flow structure and momentum transport characteristics of turbulent vortices with initial conditions. However, due to the limitation of their detection scheme, they could not provide any information on the dependence of organized structures other than the large-scale ones on the initial conditions. The question how the initial conditions produce an effect on the turbulent structure of various scales in a near turbulent wake is still open. It is suspected that the organized structures of various scales all contribute to the dependence of the turbulent topology and transport characteristics on the initial conditions.

The present work aims to study the effect of initial conditions on the turbulent structures of various scales. Measurements were conducted in the near-wake generated by a circular cylinder and a screen of 50% solidity, respectively. The wavelet multi-resolution analysis is used to decompose the measured velocity data into a number of wavelet components based on their central frequencies, which represent the turbulent structures of different scales. The flow structure of various scales is characterised and visualized by the sectional streamlines and vorticity contours of the decomposed wavelet components. The contributions the wavelet components make to the time-averaged Reynolds stress and the root mean square vorticity are estimated and compared between the two wake generators.

2. Wavelet Multi-resolution Analysis

2.1 Two-dimensional Orthogonal Wavelet Transform

Consider a two-dimensional vector function, $\vec{f}(x_1, x_2)$, and the isotropic mother wavelet, $y(x_1, x_2)$. The family of wavelet functions $y_{b_1, b_2, a}(x_1, x_2)$, which is translated by position parameters (b_1, b_2) and dilated by a scale parameter a, is given by

$$y_{b_1, b_2, a}(x_1, x_2) = \frac{1}{a} y\left(\frac{x_1 - b_1}{a}, \frac{x_2 - b_2}{a} \right)$$ (1)

where y satisfies the admissibility condition

$$C_y = \int_{-\infty}^{\infty} \int_{-\infty}^{\infty} \frac{\left| y(w_1, w_2)^2 \right|}{\left(w_1^2 + w_2^2 \right)^{1/2}} \, dw_1 dw_2 < \infty$$ (2)

where y is Fourier transform coefficient of y, and w_1 and w_2 represent frequencies. The 2-dimentional Morelet and Halo functions are frequently used as y in fluid mechanics.

The 2-dimentional continuous wavelet transform of $\vec{f}(x_1, x_2)$ can be defined as

$$\overrightarrow{Wf}(b_1, b_2, a) = \frac{1}{a} \int_{-\infty}^{\infty} \int_{-\infty}^{\infty} \vec{f}(x_1, x_2) y\left(\frac{x_1 - b_1}{a}, \frac{x_2 - b_2}{a} \right) dx_1 dx_2$$ (3)

The wavelet transform coefficients, $\overrightarrow{Wf}(b_1, b_2, a)$, may be interpreted as the contribution to the original vector function $\vec{f}(x_1, x_2)$ from the component of the scale a at the position (b_1, b_2).

Provided that the mother wavelet is admissible, the inverse wavelet transform is given by

$$\vec{f}(x_1, x_2) = \frac{1}{C_Y} \int_{-\infty}^{\infty} \int_{-\infty}^{\infty} \int_0^{\infty} a^{-4} \overrightarrow{Wf}(b_1, b_2, a) y\left(\frac{x_1 - b_1}{a}, \frac{x_2 - b_2}{a}\right) da\, db_1 db_2 \tag{4}$$

However, it is difficult to apply the two-dimensional continuous wavelet transform for the analysis of the vector field, due to its non-orthogonal decomposition. Therefore, the orthogonal or discrete wavelet transform is preferred in this study. Since the wavelet function $\frac{1}{a} y\left(\frac{x_1 - b_1}{a}, \frac{x_2 - b_2}{a}\right)$, used to define the continuous wavelet transform, forms a non-orthogonal basis, an orthogonal basis may be obtained from this function by subsampling a, b_1 and b_2. Choose the integer (positive and negative) power of one fixed dilation parameter $a_0 > 1$, that is, a_0^m, where m represents the width of wavelets. It follows that the discretization of b depends on m: narrow wavelets (high frequency) and wide wavelets (lower frequency) are translated by small and large steps, respectively, in order to cover the whole field. Since the width of wavelets is proportional to a_0^m, we choose b to be discretized, viz. $b = nb_0 a_0^m$, where b_0 is fixed. Starting from one-dimensional wavelet basis $y_{m,n}(x) = a_0^{-m/2} y(a_0^{-m}x - nb_0)$, the two-dimensional wavelet basis is simply formed by the tensor product functions of two one-dimensional bases, viz.,

$$Y_{m; n_1, n_2}(x_1, x_2) = y_{m, n_1}(x_1) y_{m, n_2}(x_2) \tag{5}$$

With $y(x)$ and a_0, b_0 carefully chosen, $y_{m,n}(x)$ may constitute an orthogonal basis. Particularly, given $a_0 = 2$ and $b_0 = 1$, we may form a two-dimensional orthogonal basis with good physics-frequency localization properties, viz.,

$$Y_{m; n_1, n_2}(x_1, x_2) = 2^{-m} y\left(2^{-m} x_1 - n_1\right) y\left(2^{-m} x_2 - n_2\right) \tag{6}$$

In the basis the two variables x_1 and x_2 are dilated separately. The Haar function is perhaps the first $y(x)$, based on which the orthogonal basis, $y_{m,n}(x)$, was constructed even long before the term "wavelet" was invented. In the last decade, various orthogonal wavelet bases have been constructed, including Meyer basis, Daubechies basis, Coifman basis, Battle-Lemarie basis and Baylkin basis and spline basis, which provide good localization properties in both physical and frequency spaces.

The two-dimensional discrete vector wavelet transform is defined based on $Y_{m; n_1, n_2}(x_1, x_2)$, viz.,

$$\overrightarrow{Wf}_{m; n_1, n_2} = \sum_i \sum_j \vec{f}\left(x_1^i, x_2^j\right) Y_{m; n_1, n_2}\left(x_1^i, x_2^j\right) \tag{7}$$

The original vector function is reconstructed from the inversion of $\overrightarrow{Wf}_{m; n_1, n_2}$

$$\vec{f}(x_1, x_2) = \sum_m \sum_{n_1} \sum_{n_2} \overrightarrow{Wf}_{m; n_1, n_2} Y_{m; n_1, n_2}\left(x_1, x_2\right) \tag{8}$$

2.2 Vector Wavelet Multi-resolution Analysis

Since the discrete wavelet transform is a linear transform, the wavelet multiresolution analysis is used to convert a non-linear problem to the superposition of a number of subsets of different central frequencies (from low frequency to high frequency). Thus, Equation (8) can be written as

$$\vec{f}(x_1, x_2) = \overrightarrow{fw}_1 + \overrightarrow{fw}_2 + \cdots + \overrightarrow{fw}_k \tag{9}$$

where

$$\overrightarrow{fw}_j = \sum_{n_1} \sum_{n_2} \overrightarrow{Wf}_{j; n_1, n_2} \Psi_{j; n_1, n_2}\left(x_1, x_2\right) \tag{10}$$

On the right side of Eq. (9), the first term $\overrightarrow{fw}_1$ and the last $\overrightarrow{fw}_k$ represent the components at level 1 (the lowest frequency) and level k (the highest frequency).

The wavelet multi-resolution analysis can be summarized in two steps:

(1) Wavelet coefficients are computed based on the discrete wavelet transform of Eq. (7).

(2) Inverse wavelet transform of Eq. (10) is applied to wavelet coefficients at each wavelet level, and components are obtained at each level or scale.

In this study, we use the Daubechies family with index $N = 20$, which is not only orthogonal, but also has smoothness and compact support, as the orthogonal wavelet basis.

3. Experimental Setup

Experiments were conducted in an open-return low-turbulence wind tunnel with a 2.4 m-long working section (0.35×0.35 m). The bottom wall was tilted to achieve a zero streamwise pressure gradient. Figure 1 shows the experimental arrangement. A circular cylinder and a screen of 50% solidity with the same height ($h = 12.5$ mm) were used to generate the wake, respectively; each was installed in the mid-plane and spanned the full width of the working section, 0.20 m from the exit plane of the contraction. This resulted in a blockage of about 3.6%. The stream-wise length of screen is about 0.5 mm. Measurements were made at $x/h = 20$ (x is the streamwise distance downstream of the cylinder) and a constant free stream velocity ($U_0 = 6.7$ m/s). The corresponding Reynolds number

$$Re \ (\equiv U_0 h/v) \text{ was 5600. The Kolmogorov length scale, which is given by } h = \left(\frac{v^3}{e}\right)^{\frac{1}{4}} = \left(\frac{v^3}{5v\left(Du/Dx\right)^2}\right)^{\frac{1}{4}},$$

was estimated to be about 0.16 mm. Where the streamwise fluctuation velocity u was measured by hot-wire and $Dx = -\overline{U}Dt$ (Taylor's hypothesis), $\overline{U}$ is the local mean velocity and Dt is the time interval between successive data points.
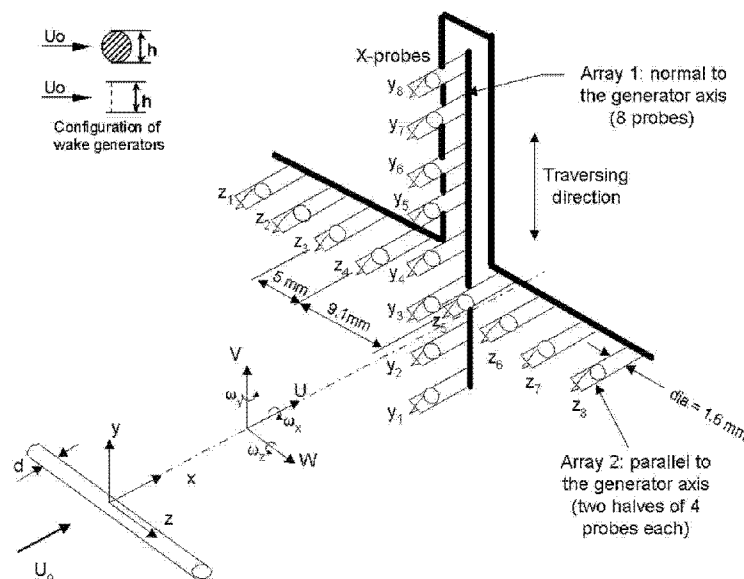

Fig. 1. Experimental setup.

Two orthogonal arrays, each consisting of eight X-wires, were used. One was aligned in the (x, y)-plane, i.e., the plane of mean shear, and the other in the (x, z)-plane, which was parallel to both the cylinder axis and the streamwise direction. The sixteen X-wires of the two arrays allow velocity fluctuations u and v in the (x, y)-plane and u and w in the (x, z)-plane to be obtained simultaneously. The nominal spacing between X-wires in both planes was about 5 mm except for a relatively large gap ($= 9.1$ mm) between the fourth and fifth X-wires in the (x, z)-plane. The arrays were attached to separate traversing mechanisms and could be moved independently of each

other. The physical blockage caused by these arrays, cables and supports was estimated to be about 3%. Several types of measurements (Zhou and Antonia, 1994b) indicated that the interference to the flow due to the two arrays was negligible. Wollaston (Pt-10% Rh) wires, 5 *m*m in diameter and about 1 mm in working length, were operated with constant temperature circuits. Signals from the circuits were offset, amplified and then digitized using two 16 channel (12 bit) A/D boards and two personal computers at a sampling frequency of f_s = 3.5 kHz per channel (the cut-off frequency was 1600 Hz). The wires were calibrated for velocity and yaw, and continuously checked for drift. Using velocity and yaw calibrations, signals proportional to u, v and w, together with the local mean velocities $\overline{U}$, $\overline{V}$ (≈ 0) and $\overline{W}$ (≈ 0), were formed on a digital tape. The duration of each record was about 38 sec.

4. Wavelet Decomposition Method of Turbulent Structures

An instantaneous velocity $U_i(x, y, z, t)$ can be written as the sum of a time-averaging component $\overline{U}_i(x, y, z)$ and a wavelet component $u_i(x, y, z, t)$, viz.

$$U_i\left(x,y,z,t\right) = \overline{U}_i\left(x,y,z\right) + u_i\left(x,y,z,t\right) \tag{11}$$

where the subscript i represents the wavelet component or wavelet level.

In order to gain insight into the turbulent structures of various scales, the wavelet multi-resolution technique is used to decompose the velocity fluctuation component $u_i(x, y, z, t)$ into a number of wavelet components based on wavelet levels, which correspond to the central frequencies and are directly linked to the turbulent structure scales. Each wavelet component represents the turbulent structures of a certain range of frequencies (i.e. a non-zero frequency band) so that the information of any scales contained in the original data will not be lost because of a limited number of wavelet levels. In the present study, thirteen wavelet levels are obtained, $u_i(x, y, z, t)$ being given by

$$u_i\left(x,y,z,t\right) = \sum_{i=1}^{13} u_{i,j}\left(x,y,z,t\right) \tag{12}$$

where $u_{i,j}(x, y, z, t)$ is the wavelet component of $u_i(x, y, z, t)$ at the jth wavelet level. Accordingly, the instantaneous velocity of the jth wavelet level is given by

$$U_{i,j}\left(x,y,z,t\right) = \overline{U}_i\left(x,y,z\right) + u_{i,j}\left(x,y,z,t\right) \tag{13}$$

The wavelet components of spanwise vorticity may be computed based on velocity data at each wavelet level using the central difference approximation. Thus, the eight X-wires in the (x, y)-plane may produce the thirteen wavelet components of spanwise vorticity at each of the seven midpoints between adjacent X-wires. The wavelet component of spanwise vorticity at the jth wavelet level may be approximated by

$$W_{zj} = \frac{\partial V_j}{\partial x} - \frac{\partial U_j}{\partial y} = \frac{\partial v_j}{\partial x} - \frac{\partial\left(\overline{U} + u_j\right)}{\partial y} \approx \frac{Dv_j}{Dx} - \frac{D\left(\overline{U} + u_j\right)}{Dy} \tag{14}$$

where $U_j = \overline{U} + u_j$ and $V_j \approx v_j$ ($\overline{V} \approx 0$). In Eq. (14), Dy (≈ 5.0 mm) is spacing between two X-wires in the (x, y)-plane; $Dx = -U_c Dt$. For simplicity, the average vortex convection velocity $U_c = 0.87U_0$ on the vortex path (Zhou and Antonia, 1992) is used to calculate Dx. Vorticity contours and rms values thus obtained showed no appreciable difference from those obtained using the local mean velocity.

5. Results and Discussion

The lateral distribution of time-averaged velocity $\overline{U}$, which depends on the initial conditions, is shown in Fig. 2. The maximum velocity deficit of the screen wake is larger than that of the cylinder wake. Figure 3 shows the power spectrum of the v-signal at y/h = 0.7, which is approximately on the vortex path. The spectrum exhibits a prominent peak around the frequency f_0 = 109 Hz and 145 Hz for the circular and screen wakes, respectively. Evidently, the frequency f_0 represents the average frequency of the large-scale vortical structures, i.e., Kármán vortices.
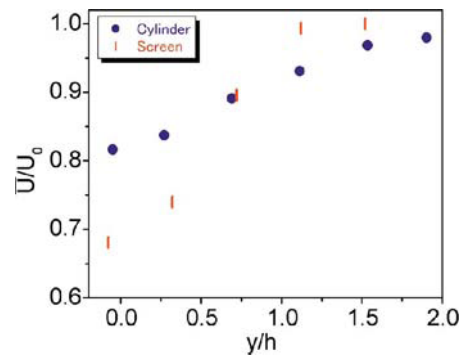
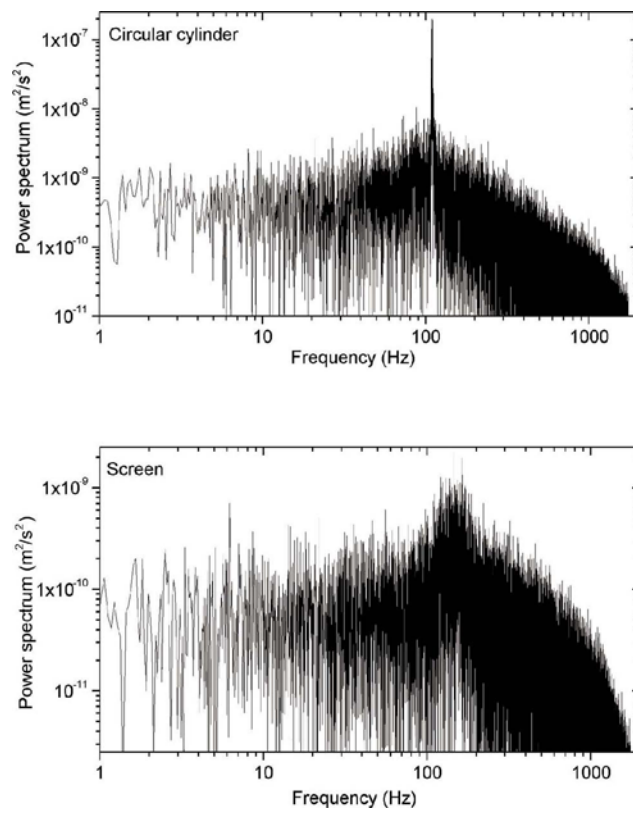Fig. 2. Lateral distribution of the mean velocity.

Fig. 3. The *v*-specturm at *y*/*h* = 0.7.

5.1 Turbulent Structures of Various Scales

In order to 'visualize' instantaneous turbulent structures of various scales, sectional streamlines (Perry and Chong, 1987) were constructed for each wavelet component of velocity as well as for measured velocities. Figure 4 shows the instantaneous sectional streamlines superimposed on the contours of normalized vorticity, w_zh/U_0, in the circular cylinder and screen wakes in the (x, y)-plane for the measured data. The timescale is increasing from left to right in such a way that the flow is observed moving from right to left. The vortical structures exhibit striking difference in geometrical shape, size, and spacing between the two wake generators. The maximum strength of spanwise vorticity in the circular cylinder wake is larger than that in the screen wake. However, only the large-scale structures are evident. It would be difficult to study the behaviours of the structures other than the large-scale ones for either flow.
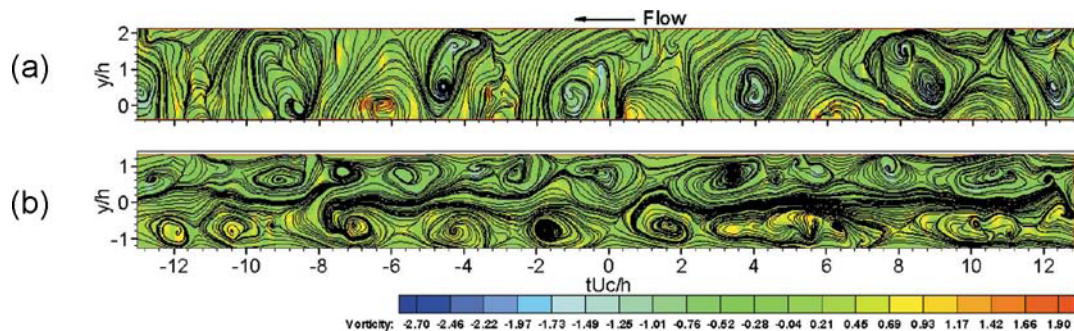
Fig. 4. Measured sectional streamlines and vortcity contours, $\omega_z h/U_o$, in the (x,y)-plane: (a) cylinder; (b) screen.

Figures 5-8 present sectional streamlines and vorticity contours of different scales in the (x, y)-plane for the circular cylinder and screen wakes, calculated from the wavelet components of velocity at the central frequencies of f_0, $2f_0$, $4f_0$ and $8f_0$. As discussed above, f_0 corresponds to the vortex shedding frequency of the circular cylinder and screen wakes, indicated by the prominent peak in the v-spectrum (in Fig. 3). Perry and Chong (1987) proposed to use the theory of critical points to describe eddy motions and flow patterns. Zhou and Antonia (1994b) successfully applied this theory to studying the topological details and three-dimensional aspects of a turbulent wake. Critical points, in particular, foci and saddle points, represent the major topological characteristics of the flow. In general, the foci of the streamlines coincide with the local vorticity peaks, suggesting that information about the flow structure can be obtained by examining either streamlines or vorticity.

Figure 5(a) displays six vortical structures in the cylinder wake, corresponding quite well to the large-scale structures in Fig. 4(a). The foci and saddle points, as denoted by F and S in Fig. 5, respectively, coincide approximately with those in Fig. 4 associated with large-scale structures, but the structures in Fig. 5 appear better organized and exhibit a much stronger periodicity. The observation indicates a correspondence between the wavelet component of the central frequency f_0 and the large-scale Kármán vorticies. Figure 5(b) exhibits nine pairs of vortices in the screen wake. These structures correspond quite well to the large-scale structures in Fig. 4(b), and their occurrence is rather periodical. They are apparently the uppermost and energy-containing structures. Again, we see a great difference in vortical structures between the two wakes. The structures in the circular cylinder wake are larger than those in the screen wake. Furthermore, the vortices in the screen wake are elliptical in shape. The maximum strength of spanwise vorticity in the circular cylinder wake, however, is smaller than that in the screen wake. These differences reflect basic differences in the vortex formation mechanisms. The vortices in the circular cylinder wake originate from the boundary layer separation from the cylinder. On the other hand, those in the screen wake are likely to arise from the shear layer instability in the developing wake. While the former, when advected downstream, are characterized by a decaying strength, the latter may have an increasing strength in the near wake (Zhang and Zhou, 2001).

As the central frequency increases to $2f_0$ (Fig. 6), we see the structures of higher frequency but smaller size than those in Fig. 5. Some of them are apparently associated with the large-scale vortices of f_0 (Fig. 5), for example, at $tU_c/h \approx -1.2$ and -4.6 in the circular cylinder wake and at $tU_c/h \approx -8$ and -8.8 in the screen wake. Others correspond to the saddle region between the large-scale vortices, such as at $tU_c/h \approx -7.2$ and 6.6 in the circular cylinder wake and at $tU_c/h \approx -6.4$ and -7.0 in the screen wake. The latter structures are consistent with the occurrence of longitudinal or rib structures, which occur between successive spanwise structures (e.g., Hussain and Hayakawa, 1987; Zhou and Antonia, 1994b; Zhang et al., 2000). The size of the vortical structure and the maximum strength of spanwise vorticity in the circular cylinder wake appear larger than that in the screen wake.

Once the central frequency reaches $4f_0$ (Fig. 7), the structures of smaller scale appear all over the flow. The structures in the circular cylinder wake appear considerably larger than those in the screen wake. The structures appear to have positive and negative vorticity concentrations aligned periodically along the flow direction. This periodicity appears to be stronger in the screen wake than in the cylinder wake.

At the central frequency of $8f_0$, the vorticity concentrations (Fig. 8) appear in strips, running spanwise. We see the wavy patterns of structures. However, the difference in the vortical structure appears diminishing between the two wakes. This is consistent with the perception that small-scale structures may be less dependent on the initial conditions.
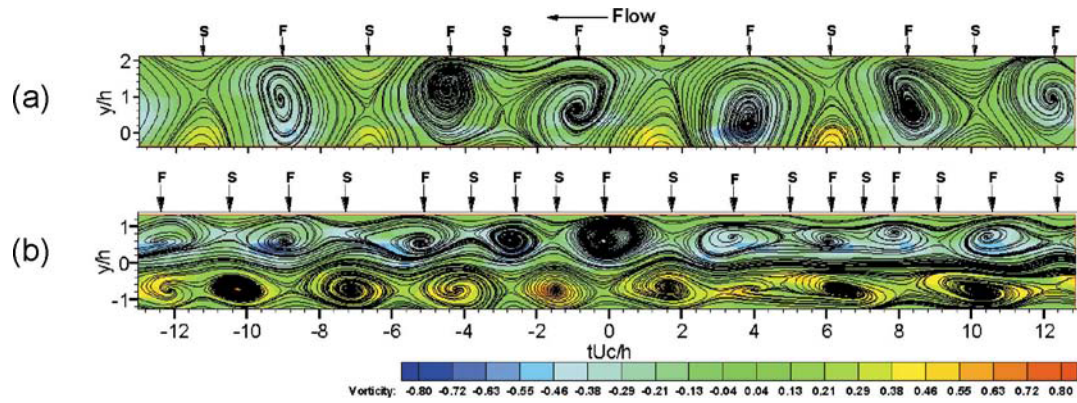
Fig. 5. Sectional streamlines and vortcity contours, $(W_z)_f$, h/U_0, of the wavelet component at f_0 in the (x, y)-plane: (a) cylinder; (b) screen.
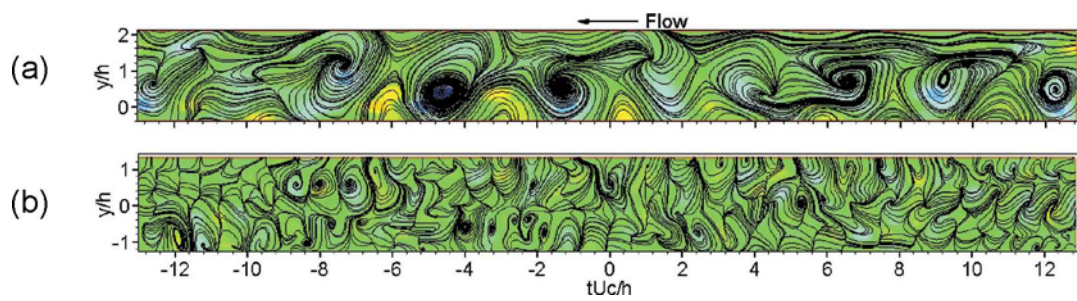

Fig. 6. Sectional streamlines and vortcity contours, $(\omega_z)_{2f}$, h/U_0, of the wavelet component at $2f_0$ in the (x, y)-plane: (a) cylinder; (b) screen. The color legend is as in Fig. 5.
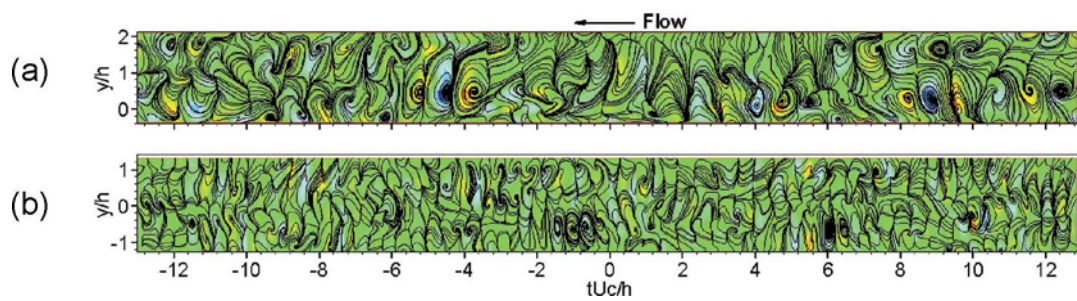

Fig. 7. Sectional streamlines and vortcity contours, $(\omega_z)_{4f}$, h/U_0, of the wavelet component at $4f_0$ in the (x, y)-plane: (a) cylinder; (b) screen. The color legend is as in Fig. 5.
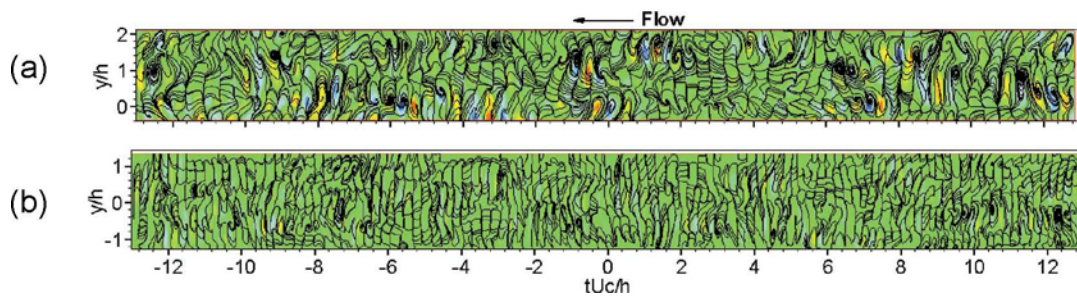

Fig. 8. Sectional streamlines and vortcity contours, $(\omega_z)_{8f}$, h/U_0, of the wavelet component at $8f_0$ in the (x, y)-plane: (a) cylinder; (b) screen. The color legend is as in Fig. 5.

5.2 Contributions to the Reynolds Stresses and Vorticity Variance from Different Wavelet Components

The wavelet components of the time-averaged Reynolds stress and root mean square (rms) vorticity u_j^2, v_j^2, u_jv_j and w_j^2, represent the contributions from the turbulent motions of various scales to the Reynolds stresses and vorticity. They are calculated from the wavelet components of instantaneous velocity and vorticity and compared between different central frequencies.

5.2.1 Reynolds stresses

Figure 9 presents the lateral distributions of u_j^2, v_j^2 and u_jv_j, as compared with the measured values for the circular cylinder and screen wakes. The results are normalized by the maximum value of the measured $(fg)_{max}$, where f or g each represents u or v, so as to indicate the contribution from each wavelet level or central frequency to the Reynolds stresses. The negative $u_jv_j/(uv)_{max}$ near $y/h = 0$ and at relatively high central frequencies has been removed in Fig. 9(c) to allow the log-scale presentation. The $(fg)_{max}$ values (Table 1) show discernible difference between the circular-cylinder and the screen wakes, in particular for $(u^2)_{max}$ and $(v^2)_{max}$. The observation is in consistence with the results of Zhou and Antonia (1994a), suggesting the effect of different generators. The wavelet component of the central frequency f_0 represents the large-scale vortical structures. The distributions of $f_jg_j/(fg)_{max}$ are similar to that of the measured data for both circular cylinder and screen, varying greatly with the central frequency. For $y/h > 1.2$, $f_jg_j/(fg)_{max}$ of the screen wake is smaller than that of the circular cylinder wake and tends to fall off quickly, approaching zero. The $f_jg_j/(fg)_{max}$ value of f_0 in the screen wake is larger than that in the circular cylinder wake for $y/h < 1.0$ (not so evident in Fig. 9 because of the use of log scale). The observation suggests that the coherent contribution from the large-scale vortical structures to the Reynolds stresses is larger in the porous body near-wake than in the solid body near-wake. The result again confirms the conception that the large-scale vortical structures contribute to the effect of initial conditions on the near wake. Furthermore, the difference between the two wakes is appreciable down to the wavelet components of $4f_0$, suggesting that the intermediate-scale structures also play a role in the persistence of the initial conditions. In general, the value of $f_jg_j/(fg)_{max}$ decreases as the central frequency increases, being consistent with the perception that the lower frequency eddies are energy-containing. For the central frequency greater than $4f_0$, $f_jg_j/(fg)_{max}$ tends to fall off quickly, approaching zero.
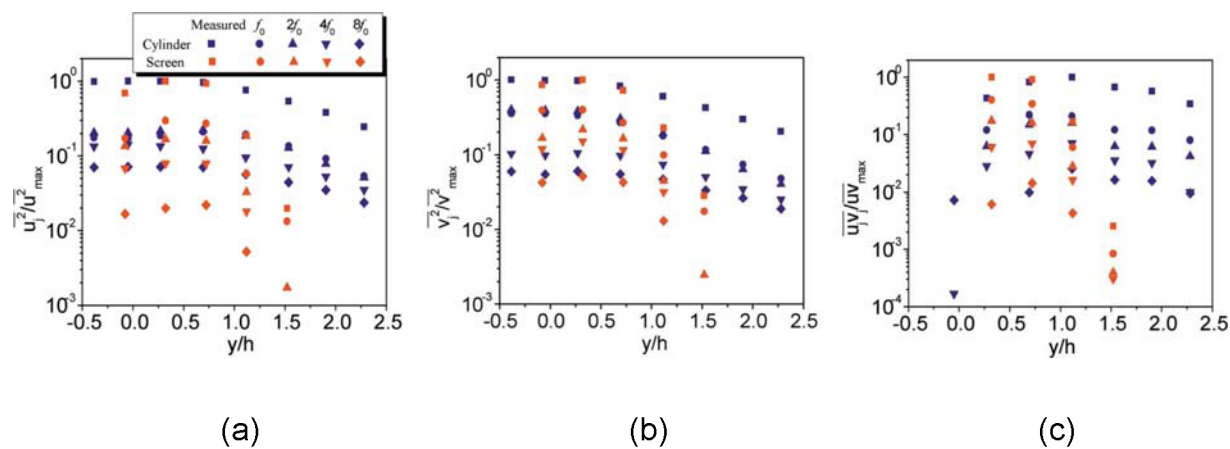

(a)   (b)   (c)

Fig. 9. Velocity variance of the measured and the wavelet components at various central frequencies.

Table 1. Maximum values of u^2, v^2, uv and w_z^2.

	$(u^2)_{max}$	$(v^2)_{max}$	$(uv)_{max}$	$(w_z^2)_{max}$
Circular cylinder	0.635	1.137	−0.102	0.106
Screen	0.220	0.176	−0.098	2.947×10^{-2}

In the case of the circular cylinder wakes, $u_j^2/(u^2)_{max}$ and $v_j^2/(v^2)_{max}$ of $2f_0$ are very close to that of f_0, implying that energies associated with the two central frequencies are quite comparable. As a matter of fact, the former even exceeds, though slightly, the latter near the centreline. This is because the lateral spacing between the two rows of vortices is small in the near-wake and thus the most prominent peak in the fluctuating velocity spectra (not shown) occurs at the second harmonic of the vortex shedding frequency near the centreline. Furthermore, the wavelet components at f_0 and $2f_0$ are most energy-containing; they account for almost 43%, 74% and 40% of $(u^2)_{max}$, $(v^2)_{max}$ and $(uv)_{max}$, respectively. This indicates a significant contribution from the intermediate-scale structures to the total Reynolds stresses. The value of the wavelet component appears falling off rather rapidly, up to about 11% of the measured value for $v_j^2/(v^2)_{max}$ when the central frequency increases from $2f_0$ to $4f_0$.

For the screen wake, $f_jg_j/(fg)_{max}$ of f_0 remains the largest value and accounts for almost 40%, 29% and 40% of $(u^2)_{max}$, $(v^2)_{max}$ and $(uv)_{max}$, respectively. The decrease is rather rapid, up to 17~22% of the measured $(fg)_{max}$, when the central frequency increases from f_0 to $2f_0$. This indicates that the greatest contribution to the total Reynolds stresses comes from the large-scale structure in the screen wake.

The above observation indicates that the most significant contribution to the Reynolds stresses comes from the turbulence structures of f_0 and $2f_0$ in the cylinder wake. However, in the screen wake, the contribution to Reynolds stresses comes primarily from the turbulence structures of f_0; the role played by those of $2f_0$ appears to be less significant than that in the cylinder wake. This is a significant difference between the two wakes.

It is pertinent to comment that $v_j^2/(v^2)_{max}$ (74%) corresponding to f_0 and $2f_0$ overwhelms $u_j^2/(u^2)_{max}$ (43%) in the cylinder wake, which is similar to the behaviour of the coherent contribution from the large-scale structures in solid bluff-body wakes (Zhou and Antonia, 1994b). In contrast, $u_j^2/(u^2)_{max}$ (40%) at f_0 exceeds $v_j^2/(v^2)_{max}$ (29%) in the screen wake, resembling the behaviour of the coherent contribution from the large-scale structures in a turbulent far-wake (Zhou and Antonia, 1994b). The different behaviours between the large-scale structures in the two wakes corroborate the proposition that their vortex generation mechanisms are not the same.

5.2.2 Vorticity variance

Figure 10 presents the spanwise measured vorticity variance $w_z^2/(w_z^2)_{max}$ and the wavelet components $w_{zj}^2/(w_z^2)_{max}$ where $(w_z^2)_{max}$, as shown in Table 1, is the maximum value of the measured vorticity. The variation of $w_{zj}^2/(w_z^2)_{max}$ with y/h is qualitatively similar to $w_z^2/(w_z^2)_{max}$. Both $w_z^2/(w_z^2)_{max}$ and $w_{zj}^2/(w_z^2)_{max}$ drop towards the free-stream. The drop is particularly fast for the screen wake. Interestingly, $w_{zj}^2/(w_z^2)_{max}$ of the circular cylinder corresponding to f_0 is now smallest, accounting for about 11% of the total vorticity variance. This indicates a relatively small contribution to the total vorticity variance from the large-scale structures. This contribution increases considerably at $2f_0$, up to about 19%, and continues to rise as the central frequency increases, reaching the maximum, about 21%, at $8f_0$. Evidently, the intermediate- and relatively small-scale structures make a major contribution to the total vorticity variance. In contrast to the cylinder wake, the difference in $w_{zj}^2/(w_z^2)_{max}$ between different central frequencies is smaller for the screen wake. The value of $w_{zj}^2/(w_z^2)_{max}$ at f_0 even reaches largest near the centerline, accounting for about 25%, though giving way to the component at $4f_0$ for $y/h \gtrsim 0.5$. This could be because vorticity is generated under the effect of the shear layer instability in the wake, irrespective of its scales. On the other hand, in the cylinder wake, the vorticity of larger scales, typically at f_0, originates from the boundary layer separation from the cylinder, while the vorticity of other scales could be due to the interactions between the large-scale structures or the effect of the shear layer instability in the wake, as in the screen wake. The observation again reflects the basic difference in the vortex formation mechanisms between the circular cylinder and screen wakes.
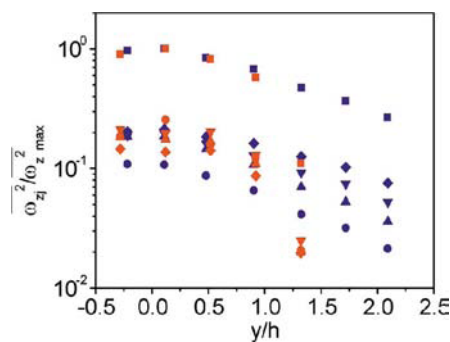

Fig. 10. Spanwise velocity variance of the measured and the wavelet components at various central frequencies. The symbols are as in Fig. 9.

6. Conclusions

(1) The vortical structures at the central frequency of f_0 are consistent with the conditionally averaged large-scale structures for both wake generators (Zhou and Antonia, 1994b). These structures, along with those of intermediate-scales, exhibit a strong dependence upon the initial conditions. However, the small-scale structures at a central frequency more than $8f_0$ are less independent of the initial conditions.

(2) The contributions to the Reynolds stresses are comparable from the turbulent structures of f_0 and $2f_0$ in the circular cylinder wake, their combined contribution accounting for 43%, 74% and 40% to $(uv)_{max}$, $(u^2)_{max}$ and $(v^2)_{max}$, respectively. In the screen wake, however, the structures of f_0 make a contribution considerably higher than other wavelet components, responsible for almost 40%, 29% and 40% to $(uv)_{max}$, $(u^2)_{max}$ and $(v^2)_{max}$, respectively.

(3) For the circular cylinder wake, the relatively small-scale structures of $8f_0$ contribute most, about 21%, to the spanwise vorticity variance. On the other hand, the large-scale structures contribute only 11% to $(w_z^2)_{max}$. This is different in the screen wake. The contribution to the vorticity variance from the structures of f_0 is quite comparable to that of other components. The above observations are consistent with the fact that the generation mechanism of the large-scale structures is different for the two wakes. While the large-scale structures in the circular cylinder wake are generated from the boundary layer separation from the cylinder, those in the screen wake may originate from the shear layer instability in the wake.

References

Charles, M., Analysis of Turbulence in the Orthonormal Wavelet Representation, Journal of Fluid Mechanics, 232 (1991), 469-520.

Farge, M., Wavelet Transforms and Their Applications to Turbulence, Annu. Rev. Fluid Mech., 24 (1992), 395-457.

Farge, M., Schneider, K. and Kevlahan, N., Non-Gaussianity and Coherent Vortex Simulation for Two-Dimensional Turbulence Using an Adaptive Orthogonal Wavelet Basis, Physics of Fluids, 11 (1999), 2187-2201.

Hussain, A. K. M. F. and Hayakawa, M., Eduction of Large-scale Organised Structures in a Turbulent Plane Wake, J. Fluid Mech., 180 (1987), 193.

Li, H., Identification of Coherent Structure in Turbulent Shear Flow with Wavelet Correlation Analysis, ASME Journal of Fluids Engineering, 120 (1998), 778-785.

Li, H. and Nozaki, T., Wavelet Analysis for the Plane Turbulent Jet (Analysis of Large Eddy Structure), JSME International Journal, Fluids and Thermal Engineering, 38 (1995), 525-531.

Li, H., Takei, M., Ochi, M., Saito, Y. and Horii, K., Application of Two-dimensional Orthogonal Wavelets to Multi-resolution Image Analysis of a Turbulent Jet, Transactions of the Japan Society for Aeronautical and Space Sciences, Vol. 42 (1999), 120-127.

Li, H., Takei, M., Ochi, M., Saito, Y. and Horii, K., Eduction of Unsteady Structure in a Turbulent Jet by Using of Continuous and Discrete Wavelet Transforms, Transactions of the Japan Society for Aeronautical and Space Sciences, Vol. 42 (2000), 39-44.

Li, H., Takei, M., Ochi, M., Saito, Y. and Horii, K., Wavelet Multiresolution Analysis Applied to Coherent Structure Eduction of a Turbulent Jet, Transactions of the Japan Society for Aeronautical and Space Sciences, Vol. 42 (2001a), 203-207.

Li, H., Hu, H., Kobayashi, T., Saga, T. and Taniguchi, N., Visualization of Multi-scale Turbulent Structure in Lobed Mixing Jet Using Wavelets, Journal of Visualization, 4-3 (2001b), 231-238.

Louchez, P. R., Kawall, J. G. and Keffer, J. F., Detailed Spread on Characteristics of Plane Turbulent Wakes, Lecture Notes in Physics, (1987), 98-109, Springer-Verlag, Berlin.

Matsumura, M., Huang, Z., Kawall, J. G. and Keffer, J. F., Coherent Structures in the Turbulent Wake of a Porous Body, Proceedings of the Eighth Symposium on Turbulent Shear Flows (1991), 28-2-1-28-2-6.

Perry, A. E. and Chong, M. S., A Description of Eddy Motions and Flow Patterns Using Critical-Point Concepts, Ann. Rev. Fluid Mech., 19 (1987), 125-155.

Screenivasan, K. R., Approach to Self-Preservation in Plane Turbulent Wakes, AIAA Journal, 19 (1981), 1365-1367.

Staszewski, W. J., Worden, K. and Rees, J. M., Analysis of Wind Fluctuations Using the Orthogonal Wavelet Transform, Applied Scientific Research, 59 (1997), 205-218.

Zhang, H. J. and Zhou, Y., Effect of Unequal Cylinder Spacing on Vortex Streets behind Three Side-by-Side Cylinders, Physics of Fluids, 13 (2001), 3675-3686.

Zhang, H. J., Zhou, Y. and Antonia, R. A., Longitudinal and Spanwise Structures in a Turbulent Wake, Physics of Fluids, 12 (2000), 2954-2964.

Zhou, Y. and Antonia, R. A., Convection Velocity Measurements in a Cylinder Wake, Experiments in Fluids, 13 (1992), 63-70.

Zhou, Y. and Antonia, R. A., Effect of Initial Conditions on Vortices in a Turbulent Near Wake, AIAA Journal, 32 (1994a), 1207-1213.

Zhou, Y. and Antonia, R. A., Critical Points in a Turbulent Near-wake, Journal of Fluid Mechanics, 275 (1994b), 59-81.

Zhou, Y. and Antonia, R. A., Memory Effects in Turbulent Plane Wakes, Experiments in Fluids, 19 (1995), 112-120.

Wygnanski, I., Champagne, F. and Marasli, B., On the Large-scale Structures in Two-dimensional, Small-deficit, Turbulent Wakes, Journal of Fluid Mechanics, 168 (1986), 31-71.

Author Profile

Hui Li: He received his two Ph.D. degrees in Department of Jet Propulsion at Beijing University of Aeronautics and Astronautics in 1989 and in Department of Mechanical Engineering at Kyushu Institute of Technology in 1993, respectively. After his Ph.D. program, he joined the Department of Mechanical Engineering at Kagoshima University as an assistant professor in 1993. He received the JSME Young Engineers Award from the Japan Society of Mechanical Engineers in 1995 and JSMF Young Engineers Award from the Japan Society for Multiphase Flow in 2001. His current research interest focuses on wavelet applications in fluid mechanics, eddy structure, two-phase flow phenomena, pneumatic conveying system and smart visualization technique. He is currently the Chairman of Topical Group on Application of Wavelets & Smart Visualization in the Visualization Society of Japan. He also served as the Organizer of Forum on Wavelet Applications in Fluid Mechanics in ASME Fluids Engineering Division Summer Meeting and the Organizer of Organized Session of Wavelet Applications & Smart Visualization in The 3rd Pacific Symposium on Flow Visualization & Image Processing and The 10th International Symposium on Flow Visualization. In addition, he has published more than 50 archival journal papers and over 80 international conference papers.

Yu Zhou: He pursued his Ph.D. degree with Prof. R. A. Antonia at The University of Newcastle (Australia) during 1989-1992. After working as a Post-Doctoral Research Fellow for one year at The University of Newcastle and another year at The University of Sydney, he joined The Hong Kong Polytechnic University in 1995 as an assistant professor and was promoted to associate professor in 2001. His research interests include turbulent flows and control, flow-induced vibrations and control. He has authored or co-authored more than 100 technical papers, including more than 40 international journal papers, among which 4 were published in the prestigious Journal of Fluid Mechanics. He has acted as a reviewer for a number of journals including Physics of Fluids, AIAA Journal, Experiments in Fluids, Journal of Fluids and Structures, International Journal of Heat and Fluid Flow and Journal of Applied Scientific Research. Since 1996, he has attracted a research fund of about 10 million HK dollars from both internal and external sources and successfully supervised 2 Ph.D. theses.